Sensors and Actuators B 248 (2017) 753–760

Contents lists available at ScienceDirect

Sensors and Actuators B: Chemical

journal homepage: www.elsevier.com/locate/snb

Research Paper

Top-and-side dual-view microfluidic device with embedded prism

Yuto Kazama[a], Edwin T. Carlen[b,c], Albert van den Berg[c], Akihide Hibara[d,e,*]

[a] Institute of Industrial Science, The University of Tokyo, Japan
[b] Graduate School of Pure and Applied Sciences, University of Tsukuba, Japan
[c] MESA+, University of Twente, The Netherlands
[d] Institute of Multidisciplinary Research for Advanced Materials, Tohoku University, Japan
[e] Department of Chemistry, Graduate School of Science, Tokyo Institute of Technology, Japan

ARTICLE INFO

Article history:
Received 24 January 2017
Received in revised form 3 March 2017
Accepted 4 April 2017
Available online 12 April 2017

Keywords:
Dual view
Microfluidic channel
PDMS
Dark-field view
Fluorescence

ABSTRACT

A polydimethylsiloxane microfluidic device enabling dual-view visualization is proposed and demonstrated. A prism with a 2 mm square base was embedded beside a 300 μm-wide microchannel. In addition to ordinary visualization from the top of the device, the microchannel could be viewed from the side, and its optical path was reflected to the top by the prism. The top and side dual visualization in a single field of view was then realized with a single objective lens. The shifts in the focal point in the top and side directions were modeled, and a compensation method utilizing a flat sheet was used. After simultaneous bright-field and dark-field visualization was attained, dual-view fluorescence imaging of the fluorescent solution and cells was realized.

1. Introduction

Microfluidic and nanofluidic systems have been enthusiastically investigated in last two decades [1–9]. The optical microscope is an important tool for studying micro- and nanofluidic devices [10–14]; it has various observation modes, such as a bright-field, dark-field, and fluorescence modes, and appropriate modes are chosen depending on the situation. For example, the dark-field mode is effective for immobilized particles.

In microfluidic investigations and applications, parameters such as three-dimensional (3D) position, shape, and deformation are often examined. One of the most common 3D imaging methods is the confocal fluorescent microscope, which can visualize microscale objects and flows with high resolution. For deformable samples such as microdroplets, the holographic 3D imaging method has been used [15,16]. For example, Oishi et al. demonstrated 3D visualization of the droplet-formation process by utilizing their digital holographic microscope. These methods utilize a coherent light source and 3D visualization is achieved with ordinary optical setups, namely a combination of an illumination path and an observation path.

Another possible 3D visualization approach is the stereoscope, with which microscale objects are observed from two different directions, without requiring a coherent light source. An ordinary binocular stereomicroscope with a slight angle difference may appear simple to our eyes, but 3D visual recording is not easy and image reconstruction methods, such as the digital image correlation method [17], are still under development. One simple way to facilitate dual-direction observation is to observe from the orthogonal directions to obtain a combined image like an orthographic projection. If orthographic-projection-like imaging is easily available, it may become a feasible option for 3D visualization.

Polydimethylsiloxane (PDMS) is widely used in microfluidic technologies and occasionally used for optofluidic devices [18,19] and for embedding small objects in microfluidic devices [20–24]. Recently, we have investigated an optics-embedding technique in PDMS microfluidic devices [25–27]. This method can potentially be applied to 3D visualization, as shown in Fig. 1. In this design, a prism is embedded beside a microchannel and an image from the side plane of the microchannel is obtained by utilizing reflection in the prism. The side-view image was obtained in our previous work [25,26], but, because of the difference between the focal lengths for the top and side observations, simultaneous top-and-side (dual) view image has not been realized.

Here we propose and demonstrate a new microfluidic device that offers simultaneous top-and-side (dual) views. The difference between the focal lengths of the top- and side-view paths is com-

* Corresponding author at: IMRAM, Tohoku University, 2-1-1 Katahira, Aoba, Sendai, 980-8577, Japan.
E-mail address: hibara@tagen.tohoku.ac.jp (A. Hibara).

http://dx.doi.org/10.1016/j.snb.2017.04.013
0925-4005/

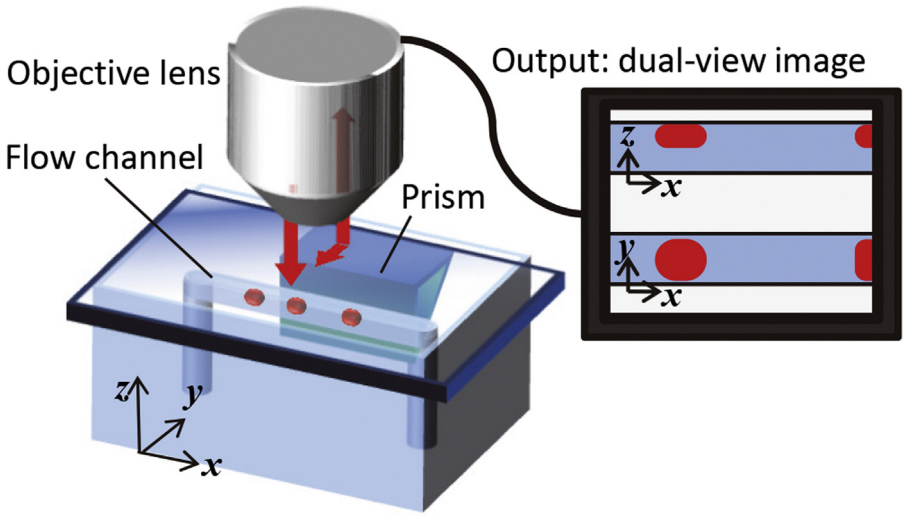

Fig. 1. Concept of dual-view flow-channel visualization. The top (*x*-*y* plane) and side (*x*-*z* plane) views are simultaneously visualized [27]. Reprinted with permission from Transducers Research Foundation. Copyright 2014.

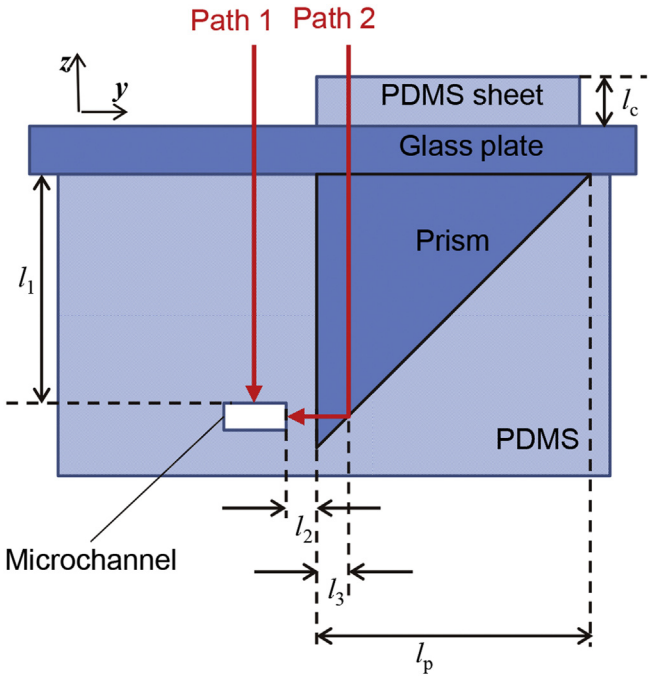

Fig. 2. Side view of the dual-view device. (For interpretation of the references to colour in the text, the reader is referred to the web version of this article.)

pensated by placing a PDMS sheet in the side-view path. First, we considered the focal lengths of the top and side paths and their deviations in different media (PDMS and prism). We then calculated the thickness of the compensating PDMS sheet, and the design was finalized. The device was fabricated, and its validity was confirmed by visualizing the microchannel.

2. Design and model

Fig. 2 shows a side view of the dual-view device. A right-angle prism is used for reflecting the optical path of the side view. In order to fix the prism on a flat surface, the prism is designed to be attached to a glass plate. The tip of the right-angle prism is then used for the reflection of the optical path of the side view to shorten the distance between the microchannel and the reflection point. Since a longer distance would lead to a wider field of view, the microchannel is not placed on the glass plate, but near the tip of the prism.

The two red lines in Fig. 2 denote the optical paths of the top and side views. For the top view (path 1), the microchannel is observed through the glass plate and the PDMS layer between the glass plate and the microchannel (thickness: l_1). For the side view (path 2), the microchannel is observed through the compensating PDMS sheet (thickness: l_c), the glass plate, the prism (side length: l_p), and PDMS layer between the prism and the microchannel (thickness: l_2). The distance between the prism surface (close to the microchannel) and the reflection point of path 2 is defined as l_3. When we ignore the height of microchannel (~several tens of micrometers), the difference between paths 1 and 2 is $l_2 + l_3$.

Despite the difference in path length, the focal lengths of the two paths can be equal by considering refraction at the interfaces. Fig. 3(a) shows a simple model for considering the focal-length shift of refractive elements. In this model, light is introduced from a medium (medium 0) with refractive index n_0 to another medium (medium 1) with refractive index n_1 and a thickness of t at an incident angle of θ. The light then exits medium 1 and re-enters medium 0. The refraction at the interfaces is described by Snell's law,

$$n_0 \sin\theta = n_1 \sin\theta', \tag{1}$$

where θ' is the refractive angle in medium 1.

After passing through medium 1, the locus deviates from the extended line of the incident light, shifting a distance of d such that

$$\frac{d}{t} = 1 - \frac{\tan\theta'}{\tan\theta}. \tag{2}$$

The numerical value of the shift divided by the thickness of medium 1, d/t, is obtained by solving the simultaneous equations. The dependence of the shift/thickness ratio on the incident angle, θ, is represented by the solid line in Fig. 3(b). It was calculated for the case of the air/PDMS interface. Generally, the shift increases for higher incident angles, which suggests that some lens structure is required for at least one of the paths in order to match the two path lengths. In contrast, in the case of a small incident angle where θ (rad) « 1, the approximation $\tan\theta \approx \sin\theta \approx \theta$ can be used and Eq. (2) is written as

$$\frac{d}{t} = 1 - \frac{n_0}{n_1}. \tag{3}$$

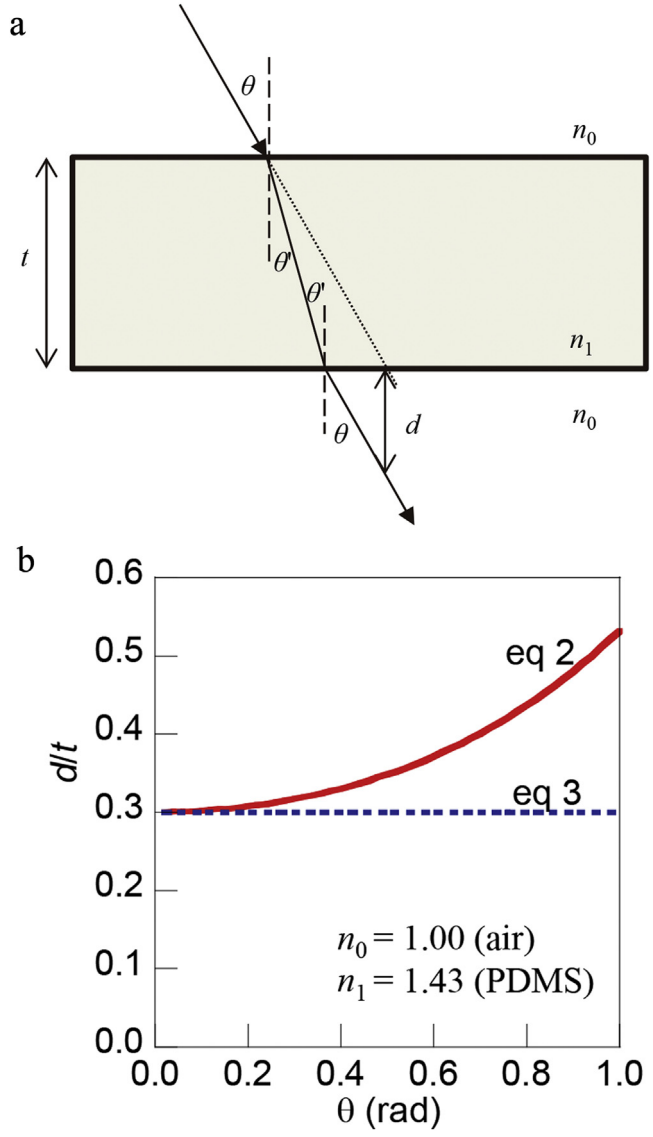

Fig. 3. (a) Simple model for considering the focal-length deviation of refractive elements. (b) Estimation of Eqs. (2) and (3).

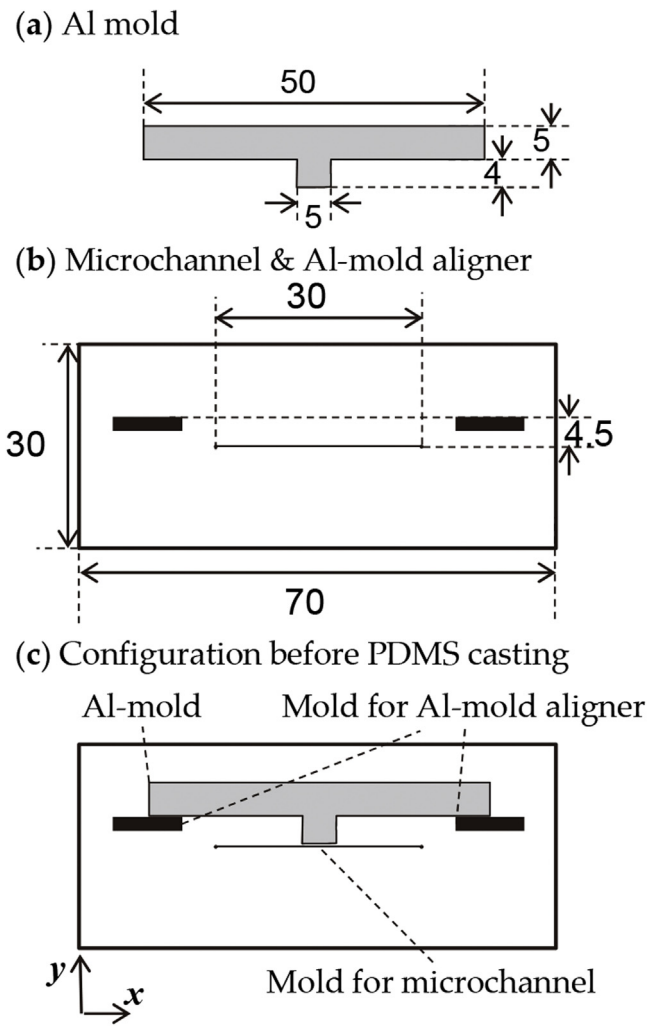

Fig. 4. (a) Top view of Al mold. (b) Microchannel and Al-mold aligner. The microchannel mold had a width of 300 μm. The distance from the top edge line of the Al-mold aligner to the center of microchannel was 4.5 mm. (c) Configuration before PDMS casting. All measurements in the diagrams are in millimeters.

In this case, the shift does not depend on the incident angle, and the shift/thickness ratio as a function of θ is represented by the broken line in Fig. 3b. When a low-magnification (e.g., 4×, 5×, and 10×) objective lens is assumed, Eq. (3) is valid. In other words, no lens structure is needed and a flat medium can compensate the focal length difference in a low-magnification dual-view system.

In the present study, we focus on the low-magnification system for a simple demonstration of our concept. The focal-length shifts of paths 1 and 2 are defined as d_1 and d_2, respectively, and calculated with Eq. (3). Here, because the shifts by the glass plate are identical in both paths, they are ignored. In path 1, only the PDMS layer should be considered and d_1 is represented by

$$d_1 = l_1 \left(1 - \frac{n_0}{n_{\mathrm{PDMS}}}\right). \tag{4}$$

In path 2, we have to consider both PDMS components (compensating sheet and layer) and the prism. The total PDMS thickness is $l_2 + l_c$ and the length of path 2 in the prism is l_p. Therefore, d_2 is represented by

$$d_2 = (l_2 + l_c)\left(1 - \frac{n_0}{n_{\mathrm{PDMS}}}\right) + l_p \left(1 - \frac{n_0}{n_{\mathrm{prism}}}\right). \tag{5}$$

As mentioned before, d_2 is longer than d_1 by $(l_2 + l_3)$. The following relationship is thus derived:

$$d_1 + l_2 + l_3 = d_2. \tag{6}$$

By solving Eq. (6), we can obtain the required PDMS sheet thickness, l_c. If a negative l_c is obtained, we have to place the PDMS sheet in path 1.

3. Experimental

3.1. Materials and apparatus

The microfluidic device with embedded optics was fabricated with soft lithography [28]. The fabrication procedures are described in the following section. A thick negative photoresist and a glass plate were used for mold preparation. The 60-μm-thick resist layer was deposited by a spin-coater, and UV light was irradiated on the parts exposed by the mask aligner. PDMS was used for mold replicating, optics embedding, and sheet preparation. To bond the PDMS layer to a glass plate or another PDMS layer, a plasma cleaner was used. A right-angle prism (N-BK7 2 mm aluminum-coated, Edmond Optics Japan) was embedded in the device. A 5-mm-thick aluminum plate was fabricated with a computer-controlled endmill. Human umbilical vein endothelial

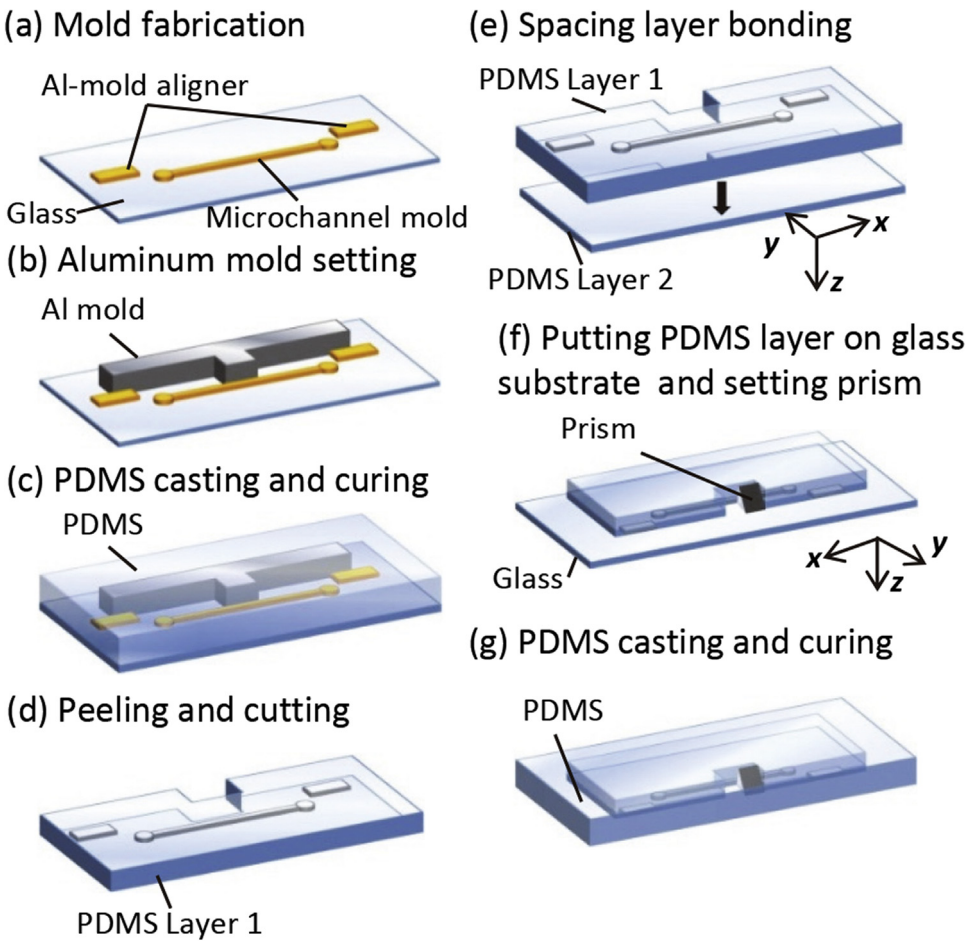

Fig. 5. Fabrication procedure for the dual-view observation microfluidic device. (a) Mold fabrication. (b) Aluminum-mold setting. (c) PDMS casting and curing. (d) PDMS peeling and cutting. (e) Spacing-layer bonding. (f) PDMS and prism setting. (g) PDMS casting and curing.

cells (HUVECs, PromoCell) were introduced to the microchannel and incubated in an endothelial cell growth medium (EGM-2, Lonza) at a temperature of 37 °C [29]. Next, the fluorescent reagents, phalloidin-fluoresceinisothiocyanate (phalloidin-FITC) for actin and hoechst for nuclei, were introduced and fluorescent micrographs were obtained. Objective lenses with magnifications of 5× (N.A. 0.10) and 10× (N.A. 0.25) were used for the observations.

3.2. Fabrication

In order to realize the design shown in Fig. 1, position control of the embedded prism is a key technology. In our study, we used the two-step PDMS-casting method. In the first step, a microchannel having a 60 μm depth was formed by an ordinary soft lithographic technique, in which an Al mold, shown in Fig. 4(a), was placed beside the microchannel. The Al mold had a square protrusion that provided the microchannel with a controlled gap. Fig. 4(b) shows the mold pattern of the microchannel with the Al-mold aligner. When the Al mold was attached to the aligner, as shown in Fig. 4(c), the distance between the protrusion and the microchannel mold matched the designed value. Here, the protrusion had a 4 mm (4000 μm) offset from the sides attached to the aligner. The aligner's side was set at a distance of 4.5 mm (4500 μm) from the center of the microchannel, and the microchannel had a width of 300 μm (the channel wall was placed 150 μm from the center line). The resulting gap of 0.35 mm (350 μm), corresponds to l_2 in Fig. 2.

This gap control process described above is illustrated in Fig. 5(a) and (b). A prepolymer liquid was cast, as shown in Fig. 5(c). After thermal solidification, the PDMS portion was peeled from the mold, and excess PDMS on the Al mold was cut to obtain a vacant notch at the original position of the square protrusion in the Al mold, as shown in Fig. 5(d) (PDMS layer 1). Another 1.8 mm-thick PDMS sheet with an identical notch and no microchannel was prepared (PDMS layer 2) as the spacing layer and bonded to the first PDMS sheet with the microchannel structure. The horizontal positions of the notches of both layers were adjusted to match (Fig. 5(e)). The thickness of PDMS layer 2 (1.8 mm) corresponds to l_1 in Fig. 2. The other side of PDMS layer 2 was bonded to a glass plate, and a right-angle prism with leg lengths of 2 mm was set in the notch, where the two perpendicular planes of the prism were attached to the PDMS plane beside the microchannel and the glass plate, as shown in Fig. 5(f). In this configuration, the bottom plane of the microchannel was at a height of 1.8 mm from the glass plate, and the prism had a side length of 2.0 mm, corresponding to l_p in Fig. 2; the value of l_3 in Fig. 2 was 0.2 mm. After the prism was set, the prepolymer liquid of PDMS was cast and cured again to embed the prim in the device.

3.3. Device

The calculation model parameters and refractive indices are summarized in Table 1. By substituting these values into Eqs. (4)–(6), we obtained a value of 1.1 mm for the thickness of the compensating PDMS sheet. Therefore, we prepared a small piece of 1.1 mm-thick PDMS sheet and bonded it to the portion through which path 2 traveled. The device is shown in Fig. 6.

Table 1
Parameters in the calculation model used to predict the thickness of the compensating PDMS sheet.

Symbol	Value
n_{PDMS}	1.43
n_{prism}	1.52
l_1	1.8 mm
l_2	0.35 mm
l_3	0.2 mm
l_p	2.0 mm
l_c	1.1 mm

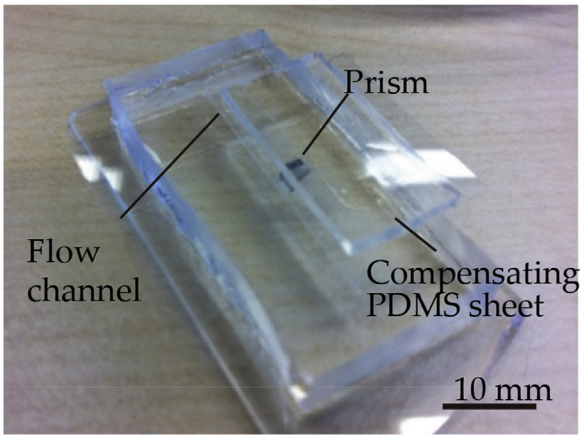

Fig. 6. Photograph of the dual-view microfluidic device.

4. Results and discussion

4.1. Observation with transillumination

The dual-view device was set on a microscope stage and observed from the top and side directions under transillumination. The illumination and observation configuration is illustrated in Fig. 7(a). The top view corresponds to ordinary bright-field observation. On the other hand, since the side-view locus is perpendicular to the illumination direction, it corresponds to dark-field observation.

Fig. 7(b) shows a micrograph, obtained with the 5× objective lens, of the area around the microchannel and the prism. The microchannel was vacant (without liquid introduction). The dark rectangular area in the upper portion of the image corresponds to the prism; the side view is also available in this section. As designed, the top and the side images were obtained in a single microscope image. As explained earlier and illustrated in Fig. 7(a), the side view yielded a dark-field image as the roughness of the microchannel wall scattered the transillumination light, and the scattered light can be seen against the dark background. The interface between the prism and PDMS can be seen between the top and side images. The image of the interface is not sharp. The image deterioration was caused by stray light, such as scattering at the edges of the channel and/or prism and multi-reflections, rather than surface roughness of the PDMS sheet and prism.

Simultaneous bright-field and dark-field observation is a notable feature of the present device. Since dark-filed observation is effective for particle analysis (microparticles, nanoparticles, cells, and so on), the device has high potential for particle analysis in microfluidic devices.

4.2. Fluorescence observation with epi-illumination

Fluorescence images of the dual-view device were obtained under epi-illumination. The illumination and observation configuration is illustrated in Fig. 8(a). The illumination light intensity should be higher in the microchannel in the dual-view area than that exiting the dual-view area because the microchannel was irradiated from the top and side directions. Fig. 8(b) shows the field of view that could be obtained with the 5× (red arrow) and 10× (blue arrow) objective lenses. The top and side images were only partially visualized with the 10× objective lens because of the wide gap between the images.

Fig. 8(c-1) shows a fluorescence micrograph, obtained with the 5× objective lens of the microchannel filled with an aqueous solution of dextran-fluorescein. The red arrow beside the image indicates the field of view and its direction in Fig. 8(b). Similar to Fig. 7(b), the top and side fluorescence images were simultaneously obtained in a single field of view. As explained earlier, the dual-view area is brighter than the other area in the top image. The bright line between the images might have been caused by scattered light at the edge of the prism.

With the 10× objective lens, the side view and the upper edge area of the top view were visualized, as shown in Fig. 8(c-2). The

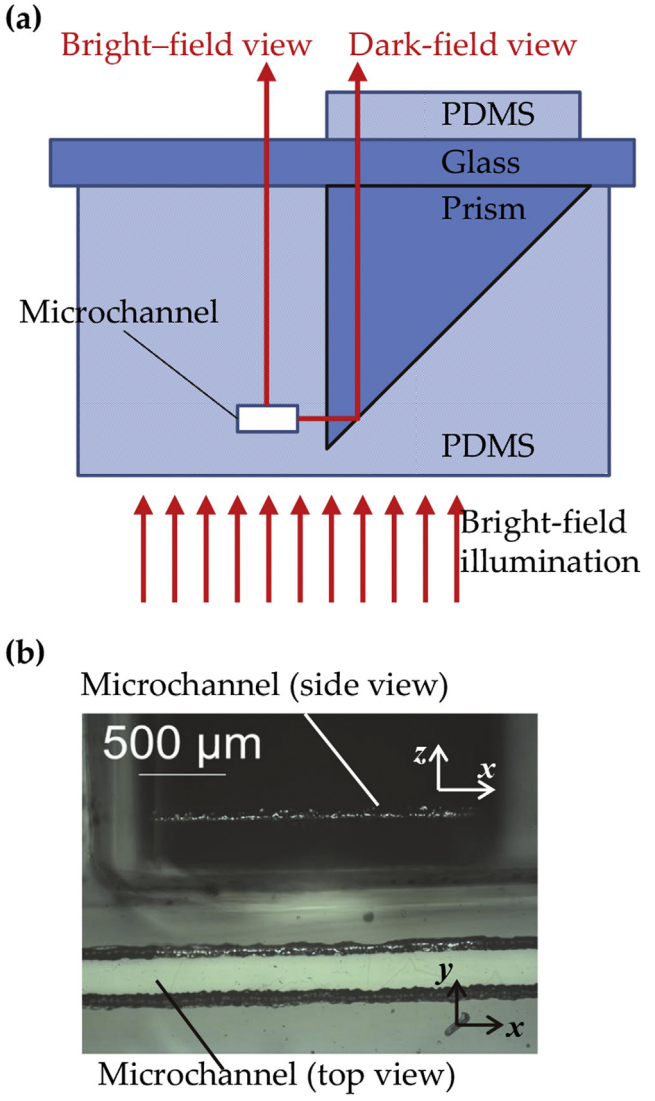

Fig. 7. (a) Characteristics of the dual-view device under transillumination. (b) Dual-view image of the device showing a vacant microchannel [27]. Fig. 7(b) is reprinted with permission from Transducers Research Foundation. Copyright 2014.

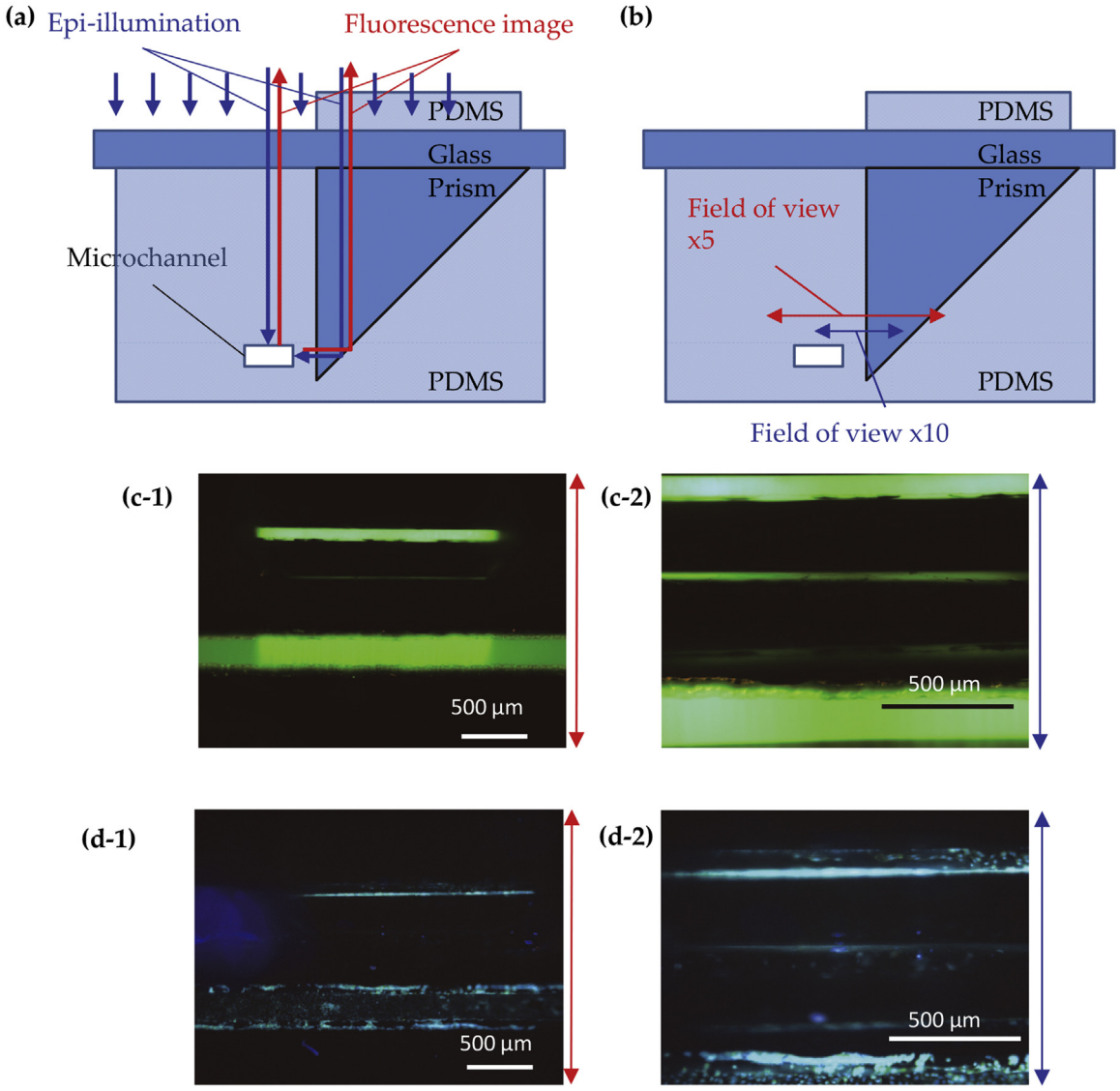

Fig. 8. (a) Characteristics of the dual-view device under epi-illumination. (b) Schematic illustration of the field-of-view ranges available with the 5× (red arrow) and 10× (blue arrow) objective lenses. Fluorescence dual-view images of the microchannel filled with aqueous dextran-FITC solution obtained with the (c-1) 5× lens and (c-2) 10× lens. Fluorescence dual-view images of the human umbilical vein endothelial cells (HUVECs) stained with phalloidin-FITC and hoechst, obtained with the (d-1) 5× lens [27] and (d-2) 10× lens. Fig. 8(d-1) is reprinted with permission from the Transducers Research Foundation. Copyright 2014. (For interpretation of the references to colour in this figure legend, the reader is referred to the web version of this article.)

image is an example of the trade-off between the resolution and the field of view, as is often the case with ordinary microscopy.

Next, HUVECs cultivated in the microchannel and stained with phalloidin-FITC and hoechst were observed. Fig. 8(c-1) shows the fluorescence image obtained with the 5× objective lens. While the size of the cells was of the order of tens of micrometers, the optical resolution was only several micrometers. Therefore, the cell images were not sufficiently resolved, but we can recognize the cell positions and their density from the image. The spotty defocused image between the top and side images might be attributed to multi-reflections in the prism.

The side view and the upper edge area of the top view were visualized with the 10× objective lens, as shown in Fig. 8(d-2). The resolution of the image is slightly improved, and we can see the attached cells on the microchannel side wall. When a higher numerical aperture is used, the focal length adjustment requires compensation with a curved surface, but it was not the case in our study, and the flat PDMS successfully compensated the focal length.

Although many issues must be resolved before our proposed technique can be effectively improved, we have successfully demonstrated dual-view visualization in a single field of view. In order to improve the resolution of the dual-view in a single image by using a higher-magnification lens, the gap between the microchannel and the prism should be shortened, and the optical path lengths should be shortened. The gap issue seems to be solved by simply using a new mold design. Smaller prisms should be used to solve the optical path length issue, and the small one with a square base of 0.2 mm × 0.2 mm is commercially available. By utilizing such a prism, the total focal length can be shortened, allowing higher-magnification observation.

5. Conclusions

Dual-view visualization in a single image of the microchannel in a microfluidic device has been proposed and successfully demonstrated based on model analysis and the use of embedded optics. We have shown that simultaneous bright-field and dark-field observation is possible by top-and-side dual-view with transillumination. Furthermore, dual-view fluorescence imaging is attainable with epi-illumination. The method is expected to contribute to microfluidic applications such as 3D cell cultures [30,31], cell deformation analysis [32], inertial microfluidics [33], magnetic applications [34], optofluidic applications [35], and droplet chemical analysis [36–39].

Acknowledgments

This work was partially supported by JSPS KAKENHI Grant Number 15H03825, by JSPS-RFBR Japan-Russia Research Cooperative Program, by the Food Nanotechnology Project of the Ministry of Agriculture, Forestry, and Fisheries of Japan, and by the Research Program of "Dynamic Alliance for Open Innovation Bridging Human, Environment and Materials" in "Network Joint Research Center for Materials and Devices". YK acknowledges the Global COE Program, Chemistry Innovation through Cooperation of Science and Engineering, MEXT, Japan and the International Training Program (ITP), Program for incubating young researchers on Plasma Nanotechnology Materials and Device Processing, JSPS for encouragement of research activities. We sincerely acknowledge Prof. Noritada Kaji and Prof. Yoshinobu Baba of Nagoya University and Dr. ir. Séverine le Gac of University of Twente for their kind support.

References

[1] A. Manz, J.C. Fettinger, E. Verpoorte, H. Lüdi, H.M. Widmer, D.J. Harrison, Micromachining of monocrystalline silicon and glass for chemical analysis systems. A look into next century's technology or just a fashionable craze? TrAC Trends Anal. Chem. 10 (1991) 144–149.
[2] D.R. Reyes, D. Iossifidis, P.A. Auroux, A. Manz, Micro total analysis systems. 1. Introduction, theory, and technology, Anal. Chem. 74 (2002) 2623–2636.
[3] P.A. Auroux, D. Iossifidis, D.R. Reyes, A. Manz, Micro total analysis systems. 2. Analytical standard operations and applications, Anal. Chem. 74 (2002) 2637–2652.
[4] H. Andersson, A. Van den Berg, Microfluidic devices for cellomics: a review, Sens. Actuators B 92 (2003) 315–325.
[5] C.T. Culbertson, T.G. Mickleburgh, S.A. Stewart-James, K.A. Sellens, M. Pressnall, Micro total analysis systems: fundamental advances and biological applications, Anal. Chem. 86 (2014) 95–118.
[6] N. Kaji, Y. Baba, Nanobiodevice-based single biomolecule analysis single-cell analysis, and *in vivo* imaging for cancer diagnosis, cancer theranostics, and iPS cell-based regenerative medicine, Anal. Sci. 30 (2014) 859–864.
[7] K. Sato, Microdevice in cellular pathology: microfluidic platforms for fluorescence *in situ* hybridization and analysis of circulating tumor cells, Anal. Sci. 31 (2015) 867–873.
[8] M. Maeki, H. Yamaguchi, M. Tokeshi, M. Miyazaki, Microfluidic approaches for protein crystal structure analysis, Anal. Sci. 32 (2016) 3–9.
[9] A. Hibara, M. Fukuyama, M. Chung, C. Priest, M.A. Proskurnin, Interfacial phenomena and fluid control in micro/nanofluidics, Anal. Sci. 32 (2016) 11–21.
[10] J. Wu, G. Zheng, L.M. Lee, Optical imaging techniques in microfluidics and their applications, Lab Chip 12 (2012) 3566–3575.
[11] S.O. Isikman, I. Sencan, O. Mudanyali, W. Bishara, C. Oztoprak, A. Ozcan, Color and monochrome lensless on-chip imaging of Caenorhabditis elegans over a wide field-of-view, Lab Chip 10 (2010) 1109–1112.
[12] V. Bianco, F. Merola, L. Miccio, P. Memmolo, O. Gennari, M. Paturzo, et al., Imaging adherent cells in the microfluidic channel hidden by flowing RBCs as occluding objects by a holographic method, Lab Chip 14 (2014) 2499–2504.
[13] N.K. Karadimitriou, P. Nuske, P.J. Kleingeld, S.M. Hassanizadeh, R. Helmig, Simultaneous thermal and optical imaging of two-phase flow in a micro-model, Lab Chip 14 (2014) 2515–2524.
[14] O. Wakao, Y. Fujii, M. Maeki, A. Ishida, H. Tani, A. Hibara, et al., Fluorescence polarization measurement system using a liquid crystal layer and an image sensor, Anal. Chem. 87 (2015) 9647–9652.
[15] M. Oishi, T. Matsuo, H. Kinoshita, T. Fujii, M. Oshima, Simultaneous measurement of 3D interfacial geometry and internal flow structure of micro droplet using digital holographic microscopy, in: Proceedings of the 18th International Conference on Miniaturized Systems for Chemistry and Life Sciences (MicroTAS 2014), San Antonio, Texas, USA, 2014, pp. 2354–2356.
[16] P. Marquet, B. Rappaz, P.J. Magistretti, E. Cuche, Y. Emery, T. Colomb, et al., Digital holographic microscopy: a noninvasive contrast imaging technique allowing quantitative visualization of living cells with subwavelength axial accuracy, Opt. Lett. 30 (2005) 468–470.
[17] T.A. Berfield, J.K. Patel, R.G. Shimmin, P.V. Braun, J. Lambros, N.R. Sottos, Micro- and nanoscale deformation measurement of surface and internal planes via digital image correlation, Exp. Mech. 47 (2007) 51–62.
[18] D. Psaltis, S.R. Quake, C. Yang, Developing optofluidic technology through the fusion of microfluidics and optics, Nature 442 (2006) 381–386.
[19] S. Xiong, A.Q. Liu, L.K. Chin, Y. Yang, An optofluidic prism tuned by two laminar flows, Lab Chip 11 (2011) 1864–1869.
[20] K. Uchiyama, W. Xu, J. Qiu, T. Hobo, Polyester microchannel chip for electrophoresis – incorporation of a blue LED as light source, Fresenius J. Anal. Chem. 371 (2001) 209–211.
[21] R.H. Cole, N. de Lange, Z.J. Gartner, A.R. Abate, Compact and modular multicolour fluorescence detector for droplet microfluidics, Lab Chip 15 (2015) 2754–2758.
[22] M.L. Chabinyc, D.T. Chiu, J.C. McDonald, A.D. Stroock, J.F. Christian, A.M. Karger, et al., An integrated fluorescence detection system in poly(dimethylsiloxane) for microfluidic applications, Anal. Chem. 73 (2001) 4491–4498.
[23] S. Camou, H. Fujita, T. Fujii, PDMS 2D optical lens integrated with microfluidic channels: principle and characterization, Lab Chip 3 (2003) 40–45.
[24] M. Rosenauer, M.J. Vellekoop, 3D fluidic lens shaping—a multiconvex hydrodynamically adjustable optofluidic microlens, Lab Chip 9 (2009) 1040–1042.
[25] Y. Kazama, A. Hibara, Integrated micro-optics for microfluidic detection, Anal. Sci. 32 (2016) 99–102.
[26] S. Yamaoka, Y. Kataoka, Y. Kazama, Y. Fujii, A. Hibara, Efficient thermal lens nanoparticle detection in a flow-focusing microfluidic device, Sens. Actuators B 228 (2016) 581–586.
[27] A. Hibara, Y. Kazama, E.T. Carlen, A. van den Berg, Dual-view flow channel visualization, in: Proceedings of the 18th International Conference on Miniaturized Systems for Chemistry and Life Sciences (MicroTAS 2014), San Antonio, Texas, USA, 2014, pp. 2342–2344.
[28] A.D. Stroock, G.M. Whitesides, Components for integrated poly (dimethylsiloxane) microfluidic systems, Electrophoresis 23 (2002) 3461–3473.
[29] A.D. van der Meer, V.V. Orlova, P. ten Dijke, A. van den Berg, C.L. Mummery, Three-dimensional co-cultures of human endothelial cells and embryonic stem cell-derived pericytes inside a microfluidic device, Lab Chip 13 (2013) 3562–3568.
[30] Y. Morimoto, S. Takeuchi, Three-dimensional cell culture based on microfluidic techniques to mimic living tissues, Biomate. Sci. 1 (2013) 257–264.
[31] S. Shin, I. Ahmed, J. Hwang, Y. Seo, E. Lee, J. Choi, et al., A microfluidic approach to investigating a synergistic effect of tobramycin and sodium dodecyl sulfate on *Pseudomonas aeruginosa* biofilms, Anal. Sci. 32 (2016) 67–73.
[32] D.R. Gossett, H.T.K. Tse, S.A. Lee, Y. Ying, A.G. Lindgren, O.O. Yang, et al., Hydrodynamic stretching of single cells for large population mechanical phenotyping, Proc. Natl. Acad. Sci. U. S. A. 109 (2012) 7630–7635.
[33] D. Di Carlo, Inertial microfluidics, Lab Chip 9 (2009) 3038–3046.
[34] C. Phurimsak, M.D. Tarn, S.A. Peyman, J. Greenman, N. Pamme, On-chip determination of C-reactive protein using magnetic particles in continuous flow, Anal. Chem. 86 (2014) 10552–10559.
[35] L. Pang, H.M. Chen, L.M. Freeman, Y. Fainman, Optofluidic devices and applications in photonics, sensing and imaging, Lab Chip 12 (2012) 3543–3551.
[36] T. Schneider, J. Kreutz, D.T. Chiu, The potential impact of droplet microfluidics in biology, Anal. Chem. 85 (2013) 3476–3482.
[37] M. Fukuyama, A. Hibara, Microfluidic selective concentration of microdroplet contents by spontaneous emulsification, Anal. Chem. 87 (2015) 3562–3565.
[38] M. Fukuyama, A. Akiyama, M. Harada, T. Okada, A. Hibara, Microfluidic protein crystallisation controlled using spontaneous emulsification, Anal. Methods 7 (2015) 7128–7131.
[39] L. Davoust, Y. Fouillet, R. Malk, J. Theisen, Coplanar electrowetting-induced stirring as a tool to manipulate biological samples in lubricated digital microfluidics. Impact of ambient phase on drop internal flow pattern, Biomicrofluidics 7 (2013) 044104.

Biographies

Yuto Kazama was a graduate student of Department of Applied Chemistry, School of Engineering, the University of Tokyo, and joined Micro Chemical System Group (Dr. Hibara's group) of Institute of Industrial Science, the University of Tokyo. He also experienced research work in Prof. van den Berg's group at University of Twente, the Netherlands for two months.

Edwin T. Carlen received the Ph.D. from the University of Michigan, USA in 2001. In 2006, he was a visiting scholar at the Institute of Physics, Leiden University, the Netherlands and later that year joined the scientific staff of the BIOS-Lab on

a Chip Group and MESA+ Institute for Nanotechnology, University of Twente, the Netherlands, as a 3TU assistant professor. He was promoted to the rank of associate professor in 2011. Currently, he is an associate professor in the Graduate School of Pure and Applied Sciences at University of Tsukuba, Japan, and leads a research group developing plasmonic devices and nanosensors.

Albert van den Berg is Full Professor on Miniaturized Systems for (Bio)Chemical Analysis in the Faculty of Electrical Engineering. He received his MSc in applied physics in 1983, and his PhD in 1988 both at the University of Twente, the Netherlands. From 1988 to 1993 he worked in Neuchatel, Switzerland, at the CSEM and the University (IMT) on miniaturized chemical sensors.

Akihide Hibara received the Bachelor, masters, and Ph. D from the University of Tokyo, Japan, in 1995, 1997, and 2003, respectively. He worked at Department of Applied Chemistry, the University of Tokyo as Research Associate (1999–2003), and Lecturer (2003–2007), and at Institute of Industrial Science, the University of Tokyo as Associate Professor (2007–2013). He worked at the Department of Chemistry, Tokyo Institute of Technology as Associate Professor (2013–2016). He works at Institute of Multidisciplinary Research for Advanced Materials, Tohoku University as Professor (2016-). His research interest is micro-/nanofluidics, liquid interface science, and laser spectroscopy.